

# MASS AND ECCENTRICITY CONSTRAINTS IN THE WASP-47 PLANETARY SYSTEM FROM A SIMULTANEOUS ANALYSIS OF RADIAL VELOCITIES & TRANSIT TIMING VARIATIONS

LAUREN M. WEISS<sup>1,9</sup>, KATHERINE M. DECK<sup>2</sup>, EVAN SINUKOFF<sup>3,10</sup>, ERIK A. PETIGURA<sup>2,11</sup>, ERIC AGOL<sup>4,5</sup>, EVE J. LEE<sup>6</sup>, JULIETTE C. BECKER<sup>7</sup>, ANDREW W. HOWARD<sup>2</sup>, HOWARD ISAACSON<sup>6</sup>, IAN J. M. CROSSFIELD<sup>8</sup>, BENJAMIN J. FULTON<sup>3</sup>, LEA HIRSCH<sup>6</sup>

*Submitted to AJ, Dec. 14, 2016.*

## ABSTRACT

Measuring precise planet masses, densities, and orbital dynamics in individual planetary systems is an important pathway toward understanding planet formation. The WASP-47 system has an unusual architecture that invites a complex formation theory. The system includes a hot Jupiter (“b”) neighbored by interior (“e”) and exterior (“d”) sub-Neptunes, and a long-period eccentric giant planet (“c”). We simultaneously modeled the K2 transit times and 118 radial velocities to determine precise masses, densities, and Keplerian orbital elements of the WASP-47 planets. For the transiting inner planetary system, we obtain  $M_e = 9.1 \pm 1.0 M_\oplus$  ( $\rho_e = 7.7 \pm 1.3 \text{ g cm}^{-3}$ ),  $M_b = 358 \pm 12 M_\oplus$  ( $\rho_b = 0.88 \pm 0.11 \text{ g cm}^{-3}$ ), and  $M_d = 13.6 \pm 2.0 M_\oplus$  ( $\rho_d = 1.5 \pm 0.3 \text{ g cm}^{-3}$ ). Combining RVs and TTVs provides a substantially better estimate of the mass of planet d ( $13.6 \pm 2.0 M_\oplus$ ) than obtained with only RVs ( $12.75 \pm 2.70 M_\oplus$ ) or TTVs ( $16.1 \pm 3.8 M_\oplus$ ). Planets e and d have high densities for their size, consistent with a history of photo-evaporation and/or formation in a volatile-poor environment. Through our RV and TTV analysis, we find that the planet orbits are profoundly circular:  $e_e < 0.06$ ,  $e_b < 0.011$ , and  $e_d < 0.025$  (95% confidence). The WASP-47 system has three similarities to our own solar system: (1) the planetary orbits are nearly circular and coplanar, (2) the planets are not trapped in mean motion resonances, and (3) the planets have diverse compositions. None of the current single-process exoplanet formation theories adequately reproduce these three characteristics of the WASP-47 system (or our solar system). We propose that WASP-47, like the solar system, formed in two stages: first, the giant planets formed in a gas-rich disk and migrated to their present locations, and second, the high-density sub-Neptunes formed in situ in a gas-poor environment.

## 1. INTRODUCTION

One of the key questions driving exoplanet science is the formation of planetary systems in general and the solar system in particular. The *Kepler* Mission (Borucki et al. 2010; Koch et al. 2010), led to a wealth of statistical measurements that provide valuable insight into planet formation. Small planets close to their stars are a common outcome of planet formation (Howard et al. 2012; Fang & Margot 2012; Batalha et al. 2013; Fressin et al. 2013; Petigura et al. 2013b; Dressing et al. 2014), such that half of sun-like stars have at least one planet smaller than Neptune within the orbital distance of Mercury (Petigura et al. 2013a; Burke et al. 2015). Many small planets close to their stars are in multi-planet systems (Lissauer et al. 2012; Fabrycky et al. 2014; Rowe

et al. 2014; Lissauer et al. 2014). Given the abundance of small, compact planetary systems around other stars, is our own solar system unusual in that it is barren from Mercury’s orbit inward? Because the *Kepler* Mission only obtained 4 years of continuous photometry and only observed 150,000 stars, it had poor sensitivity to long-period planets, which are unlikely to transit. If *Kepler* were pointed at our solar system and were lucky enough to discover the inner planets, it still most likely would have missed the planets from Mars out. How can we reconcile planet formation theory for the close-in exoplanets with planet formation theory for our sparsely spread solar system?

WASP-47 is a system of unusual architecture that might be a Rosetta Stone for linking the exoplanet population to the solar system. WASP-47 contains a transiting, Jupiter-size planet with an orbital period of 4.2 days (a “hot Jupiter”) that was detected from the ground-based WASP-South transit survey (Hellier et al. 2012, WASP-47 b). What makes WASP-47 b unusual is that, contrary to the vast majority of hot Jupiters, which do not have nearby planetary companions (Steffen et al. 2012; Bryan et al. 2016), WASP-47 b has two nearby neighbors: an interior, transiting planet with an orbital period of less than a day (WASP-47 e) and an exterior, transiting planet with an orbital period of 9.0 days (WASP-47 d). The system also has a distant, moderately eccentric planet (WASP-47 c). While the compactness of the WASP-47 inner planetary system is comparable to other *Kepler* systems, especially those that contain ultra-short period planets (Sanchis-Ojeda et al. 2013),

<sup>1</sup> Institut de Recherche sur les Exoplanètes, Université de Montréal, Montréal, QC, Canada

<sup>2</sup> California Institute of Technology, Pasadena, CA, USA

<sup>3</sup> Institute for Astronomy, University of Hawai’i at Mānoa, Honolulu, HI, USA

<sup>4</sup> Astronomy Department, University of Washington, Seattle, WA, USA

<sup>5</sup> NASA Astrobiology Institute Virtual Planet Laboratory, Seattle, WA, USA

<sup>6</sup> Astronomy Department, University of California, Berkeley, CA, USA

<sup>7</sup> Astronomy Department, University of Michigan, Ann Arbor, MI, USA

<sup>8</sup> Astronomy Department, University of California, Santa Cruz, CA, USA

<sup>9</sup> Trottier Fellow

<sup>10</sup> NSERC Fellow

<sup>11</sup> NASA Hubble Fellow

the combination of the compact planetary system with a hot Jupiter is unprecedented among the 2217<sup>1</sup> planetary systems studied to date. The architecture of WASP-47 was not predicted by planet formation theory, and so uncovering a physically plausible formation mechanism for WASP-47 will deepen our understanding of planet formation in general.

To better understand which of the various physical models of planet formation and evolution were important in the WASP-47 system, we would like to measure the masses, densities, bulk compositions, and orbital dynamics of all the planets as precisely as the current data permit. The compositions of the planets might provide clues about where they formed within the protoplanetary disk—for instance, if the planets are rich in water or other high mean-molecular weight volatiles, they might have formed beyond a molecular snowline. Furthermore, the present-day orbital elements for the planets can be related to their dynamical history: the semi-major axes and eccentricities of the planets today relate to how they have exchanged energy and angular momentum in the past.

Several analyses of this system have already characterized various dynamical properties of the WASP-47 planets. The discovery paper (Hellier et al. 2012) used two years of ground-based photometry to find WASP-47 b in transit, and also obtained 19 low-precision RVs to measure the planet’s mass. Becker et al. (2015, hereafter B15) discovered two additional transiting planets (e and d) in transits from K2, characterized the planet masses with transit timing variations, and used the Mercury N-body integrator (Chambers 1999) to explore the dynamical stability of the planets. Sanchis-Ojeda et al. (2015) measured the projected spin-orbit obliquity of the hot Jupiter via the Rossiter-McLaughlin effect, finding that the planetary orbital axis and the stellar spin axis are not strongly misaligned. Dai et al. (2015) obtained high-cadence precision RVs of the system, precisely characterizing the mass of the giant planet and placing new mass constraints on the other transiting planets. Neveu-VanMalle et al. (2016) discovered a long-period giant planet with a multi-year baseline of radial velocities. Almenara et al. (2016) simultaneously modeled the K2 light curve and the literature RVs, arriving at planet masses that were determined to a precision of  $\sim 40\%$  at best (for planet d). Sinukoff et al. 2016 (accepted), obtained 47 new RVs with Keck-HIRES, which, when combined with the literature RVs, significantly improved the precision of the mass and  $m \sin i$  measurements ( $< 25\%$ ) for all the WASP-47 planets.

We present the a robust analysis of the planet masses and orbital dynamics by combining the 108 transit times measured in B15 with 118 literature radial velocities. Our paper is structured as follows: in Section 2 we introduce the measurements analyzed herein, in Section 3 we present two ways to analyze the TTVs alone: using an N-body integrator and a dynamical analytic solver. In Section 4 we present a joint analysis to the TTVs and RVs of the WASP-47 system that results in the most accurate and precise dynamical parameters to date. In Section 5 we present a new, simple way to combine information from TTVs and RVs. In Section 6 we discuss how

TABLE 1  
PRIORS ON DYNAMICAL PARAMETERS

Parameter	Priors
$M$	$M > 0$ , Hill criterion
$P$	$P > 0$ , Hill criterion
$TT$	None
$\sqrt{e} \cos \omega$	$e < 0.06$ , Hill criterion
$\sqrt{e} \sin \omega$	$e < 0.06$ , Hill criterion
$\sqrt{e_c} \cos \omega_c$	$e < 1$ , Hill criterion
$\sqrt{e_c} \sin \omega_c$	$e < 1$ , Hill criterion

our improved mass and eccentricity information relates to planet formation theory. We conclude in Section 7.

## 2. MEASUREMENTS

The measurements we use in this analysis are all available in the literature. We combine the 108 transit times (TTs or TTVs) of WASP-47 e, b, and d (B15) with 118 measurements of the radial velocity (RV) of the WASP-47 host star from Hellier et al. (2012), Dai et al. (2015), Neveu-VanMalle et al. (2016), and S16.

To combine the RV measurements, we use the values for the RV zero-point offset ( $\gamma$ ) and jitter ( $\sigma_{\text{jit}}$ ) determined in S16. The zero-point offset is added to each RV measurement, and the jitter is added to each RV uncertainty in quadrature. For the Hellier et al. (2012) CORALIE RVs, these values are  $\gamma = 27070.3 \text{ m s}^{-1}$ ,  $\sigma_{\text{jit}} = 5.9 \text{ m s}^{-1}$ . For the Neveu-VanMalle et al. (2016) CORALIE RVs, these values are  $\gamma = 27085.3 \text{ m s}^{-1}$ ,  $\sigma_{\text{jit}} = 6.7 \text{ m s}^{-1}$ . For the Dai et al. (2015) Magellan-PFS RVs, these values are  $\gamma = 20.5 \text{ m s}^{-1}$ ,  $\sigma_{\text{jit}} = 6.3 \text{ m s}^{-1}$ . For the S16 Keck-HIRES RVs, these values are  $\gamma = 6.4 \text{ m s}^{-1}$ ,  $\sigma_{\text{jit}} = 3.7 \text{ m s}^{-1}$ . For simplicity, we keep the values of the zero-point offset and jitters fixed at the values determined in S16. The zero-point offsets and jitter are statistical properties of the RVs, and so we do not expect the TTVs to provide any new information about these parameters.

## 3. TTVS-ONLY ANALYSIS WITH N-BODY (TTVFAST) AND ANALYTIC (TTVFASTER) APPROACHES

In this section, we fit the WASP-47 TTVs as measured in B15 using two different approaches. First, we do a full N-body simulation of the three transiting planets to reproduce the observed TTVs. Then, we use **TTVfaster** (Agol & Deck 2016a,b), a publicly available code that analytically models orbits to first order in eccentricity. The **TTVfaster** code was designed to reproduce both low-frequency sinusoidal features and high-frequency “chopping” patterns in the TTVs, both of which we see in the WASP-47 TTVs. In the tests below, we determine that **TTVfaster**, which is orders of magnitude faster than **TTVfast**, is appropriate for modeling the TTVs.

### 3.1. Modeling transit times with the N-body Integrator **TTVfast**

We used the publicly available N-body integrator **TTVfast** (Deck et al. 2014) to forward-model the transit times of the inner three planets. Unlike in the B15 analysis, we allowed all of the initial osculating elements, particularly the orbital periods and initial times of transits, to vary. Thus, the variables for each planet  $k$

<sup>1</sup> Based on a 2016-11-24 query of Exoplanets.org.

TABLE 2  
DYNAMICAL PARAMETERS FROM BEST N-BODY  
FIT TO TTVs ONLY (TTVFAST)

Parameter	Median $\pm$ Std. Dev.	Units
$M_e$	$176 \pm 118$	$M_\oplus$
$M_b$	$549 \pm 252$	$M_\oplus$
$M_d$	$16.1 \pm 3.8$	$M_\oplus$
$P_e$	$0.78964 \pm 0.00002$	days
$P_b$	$4.150 \pm 0.006$	days
$P_d$	$9.12 \pm 0.05$	days
$TT_e$	$2146.7639 \pm 0.0008$	BJD - 2454833
$TT_b$	$2149.969 \pm 0.006$	BJD - 2454833
$TT_d$	$2155.40 \pm 0.05$	BJD - 2454833
$\sqrt{e_e} \cos \omega_e$	$-0.006 \pm 0.14$	
$\sqrt{e_e} \sin \omega_e$	$-0.008 \pm 0.14$	
$\sqrt{e_b} \cos \omega_b$	$0.001 \pm 0.08$	
$\sqrt{e_b} \sin \omega_b$	$0.006 \pm 0.07$	
$\sqrt{e_d} \cos \omega_d$	$-0.09 \pm 0.11$	
$\sqrt{e_d} \sin \omega_d$	$0.07 \pm 0.09$	

NOTE. — These are the initial astrometric Keplerian orbital elements, reported at epoch BJD 2456979.4961. They are not the time-averaged orbital properties of the planets.

are: the mass of the planet  $M_k$ , the orbital period  $P_k$ , a representative time of transit  $tt_k$ , and the eccentricity parametrization  $\sqrt{e_k} \cos \omega_k$ ,  $\sqrt{e_k} \sin \omega_k$ . We limited  $e < 0.06$  for the three inner planets, in accordance with the 10 Myr stability analysis in B15. For each adjacent pair of planets, we satisfied the Hill criteria for stability for low-eccentricity orbits, as described in Equations 24 and 28 of Gladman (1993):

$$p - q > 2.4(\mu_1^2 + \mu_2^2)^{1/3} \quad (1)$$

$$p - q > \sqrt{8/3(e_1^2 + e_2^2) + 9 \times \max(\mu_1, \mu_2)^{2/3}} \quad (2)$$

where the subscript 1 refers to the inner planet and 2 refers to the outer planet,  $q$  is the apoapse distance of the inner planet  $q = 1 + e_1$ ,  $p$  is the periapse distance of the outer planet  $p = (1 - e_2) \frac{a_2}{a_1}$ ,  $e$  is the eccentricity, and  $\mu$  is the planet-to-star mass ratio. We also required the planet masses and orbital periods to have positive values. Because the orbits of the planets are very nearly coplanar (Becker et al. 2015; Almenara et al. 2016), we fixed the orbital inclination and longitude of ascending node in a manner consistent with coplanar, edge-on orbits. See Table 1 for a summary of the priors and constraints.

We used the MCMC Python package *emcee* (Foreman-Mackey et al. 2013) to explore the posteriors of various combinations of the dynamical parameters. We ran 60 walkers  $5 \times 10^5$  steps each, throwing away the first  $10^5$  steps as burn-in, and checked that the multivariate extension of the potential scale reduction factor (PSRF) statistic ( $\hat{R} < 1.2$ , Gelman & Rubin 1992; Brooks & Gelman 1998) converged. We also inspected the chains by eye to check for convergence. Our best fit<sup>12</sup> to the transit times using *TTVFast* is shown in Figure 1. Table 2 summarizes our results from this N-body fit to the TTVs.

We find that, for planets e and b, the masses and eccentricities of the planets are highly covariate with the *initial osculating orbital period* and the *initial transit time*

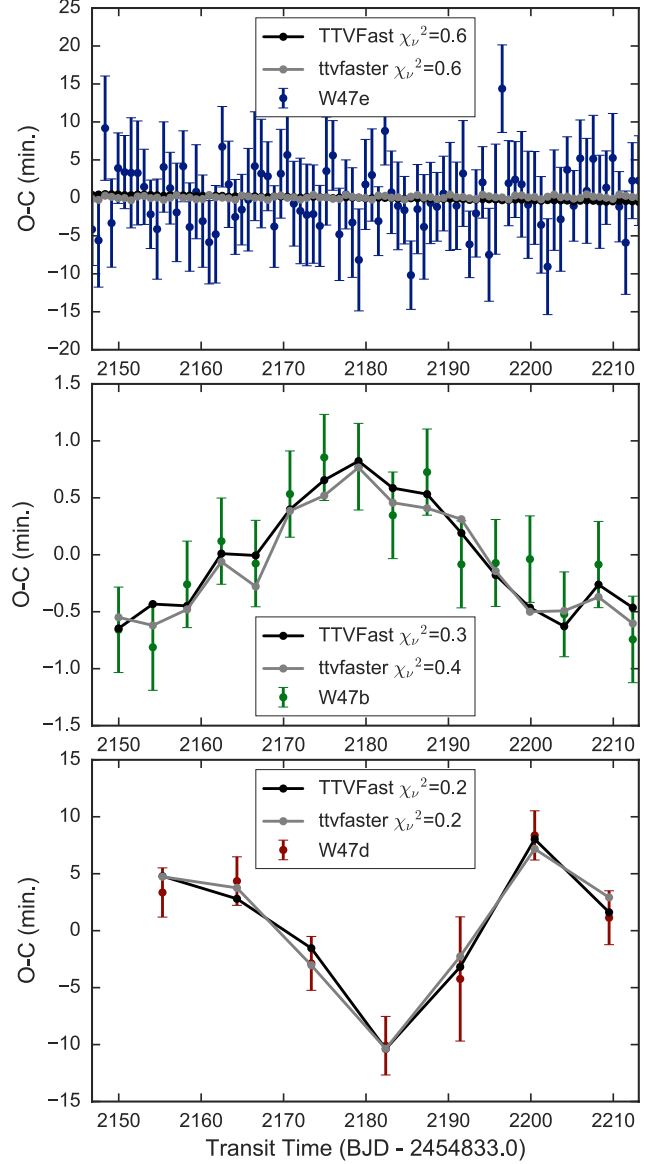


FIG. 1.— The observed minus linear-ephemeris calculated transit times of WASP-47 e (blue points, top panel), b (green points, middle panel), and d (brown points, bottom panel). The best-fit N-body model to the TTVs alone (using *TTVFast*, black connected dots) and the best-fit analytic model to the TTVs alone (using *TTVFaster*, gray connected dots) are shown.

of neighboring planets (see Figure 2). This is because the initial osculating orbital period is translated to an instantaneous velocity and acceleration, and the planet's acceleration depends on the mass and position of its neighbor. Therefore, it is critical to allow the initial orbital periods and times of transit of all the planets to vary in order to explore the full range of possible planet masses. Thus, we find that the TTVs do not constrain the masses of WASP-47 e or WASP-47 b as tightly as what is reported in B15. Whereas B15 find  $M_b = 341^{+73}_{-55} M_\oplus$ , we find  $M_b = 549 \pm 252 M_\oplus$ , using the exact same TTV measurements. The mass for planet e reported in B15 stems from their choice of prior: they find  $M_e < 22 M_\oplus$ , whereas we find  $M_e = 176 \pm 118 M_\oplus$ . However, the TTVs of planet b place strong constraints on the mass of planet d. B15 find  $M_d = 15.2 \pm 7$ , and we find  $M_d = 16.1 \pm 3.8 M_\oplus$ .

<sup>12</sup> from the MCMC maximum likelihood

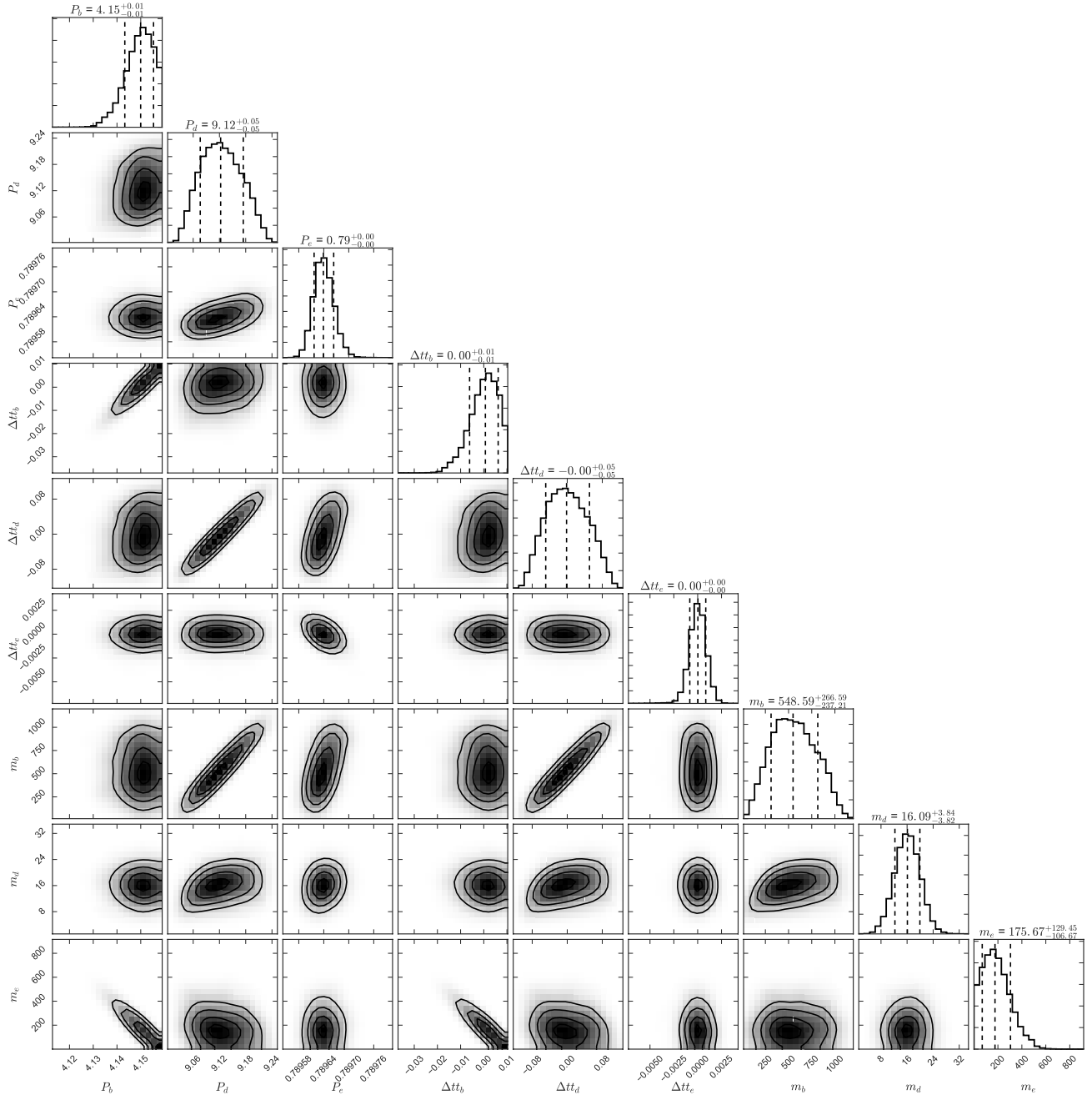


FIG. 2.— Posteriors of the planet masses, initial osculating orbital periods, and initial times of transit for WASP-47 e, b, and d in the **TTVFast** (N-body) analysis. The planet masses are highly covariant with the initial orbital elements. Note that the orbital periods and times of transit here are initial osculating elements, not the time-averaged orbital elements.

The eccentricity vectors of the planets are small and are not strongly correlated with planet mass.

### 3.2. Modeling transit times analytically with **TTVfaster**

We used the publicly available analytic TTV package **TTVfaster** to model the transit times of the inner three planets observed in B15. The **TTVfaster** code analytically transforms the planet mass  $M_k$  and average orbital elements  $P_k, tt_k, e_k \cos \omega_k, e_k \sin \omega_k$ <sup>13</sup> into a TTV pattern, to first order in eccentricity, to a user-specified precision in the disturbing function. We found that modeling to

<sup>13</sup> We used jump parameters  $\sqrt{e_k} \cos \omega_k, \sqrt{e_k} \sin \omega_k$  to avoid an eccentricity bias and speed convergence.

sixth order in the expansion of the Laplace coefficient  $b_{1/2}^j$  ( $j = \{0, 1, 2, 3, 4, 5, 6\}$ ), (Murray & Dermott 2000) was sufficient to reproduce the observed TTV signature with the same fidelity as produced in the N-body analysis (see Figure 1). In general, **TTVfaster** is designed to work for planets that (1) are not extremely close to a mean motion resonance, (2) have low eccentricities, (3) have low masses. Because WASP-47 b is a Jupiter-mass planet, we wanted to see if **TTVfaster** modeled the orbital dynamics correctly.

Incorporating the priors from Table 1, we used Python packages **lmfit** (Newville et al. 2014) and **emcee** to explore the posteriors of the dynamical parameters. We

ran 100 walkers 20,000 steps, throwing away the first 4000 steps as burn-in. We note that the chains converged much faster (according to the PSRF statistic) when we used **TTVfaster** than when we used **TTVfast**, because the TTVs provide better constraints on the average orbital parameters than they do on the initial orbital parameters.

The mass and eccentricity distributions we determined from the analytic solution to the observed TTVs are consistent with the N-body model (Figure 3). Since fitting an analytic model to the TTVs is orders of magnitude faster than a full N-body analysis (especially when the long time baseline for RVs is required), we use the analytic modeling technique in the rest of this paper.

#### 4. COMBINING TTVS AND RVs WITH TTVFASTER

We combined the python packages **TTVfaster** and **radvel** (Fulton & Petigura in prep.<sup>14</sup>) to simultaneously fit the RVs and TTVs, resulting in refined masses and orbital properties of all four known planets. To fit the RV and TTV data simultaneously, we maximized the following log-likelihood function while satisfying our priors:

$$\ln L = - \sum_i^{N_{RV}} \frac{(RV_{obs,i} - RV_{Kep,i})^2}{2\sigma_{RV,i}^2} - \sum_k^{N_{pl}} \sum_j^{N_{TT,k}} \frac{(TT_{obs,k,j} - TT_{model,k,j})^2}{2\sigma_{TT,k,j}^2} \quad (3)$$

where  $N_{RV}$  is the number of RVs;  $N_{pl}$  is the number of planets;  $N_{TT,k}$  is the number of transit times for planet  $k$ ;  $RV_{obs,i}$  is the  $i$ th observed RV, including the instrument-specific fixed zero-point offset  $\gamma$  determined in S16;  $RV_{Kep,i}$  is the  $i$ th Keplerian-modeled RV;  $\sigma_{RV,i}$  is the uncertainty in  $RV_{obs,i}$ , including a constant jitter for each spectrometer determined in S16;  $TT_{obs,k,j}$  is the  $j$ th observed transit time for planet  $k$ ;  $TT_{model,k,j}$  is the  $j$ th modeled transit time for planet  $k$ ; and  $\sigma_{TT,k,j}$  is the uncertainty in  $TT_{obs,k,j}$ .

Our model included all four known planets. The variable parameters for each planet  $k$  are: the mass of the planet  $M_k$ , the orbital period of the planet  $P_k$ , a representative time of transit  $tt_k$ , and the eccentricity parameterization  $\sqrt{e_k} \cos \omega_k$ ,  $\sqrt{e_k} \sin \omega_k$ . Note that the argument of periape passage,  $\omega_k$ , is for the planet, not the star. These parameters are transformed into the appropriate basis to drive a Keplerian RV model (for comparison to the RVs) and the basis used for **TTVfaster** computations. Note that this scheme is not possible for an N-body integrator, since the initial osculating orbital elements are not the same as the time-averaged osculating orbital elements used in a Keplerian prescription. We also required Hill stability for all the planets, as described in Equations 1 and 2. In addition, we allowed the stellar mass to vary, using the prior  $M_\star = 0.99 \pm 0.05 M_\odot$  from S16, in case the combined RV and TTV data added new information about the stellar mass.<sup>15</sup> The best simultaneous fit to the TTVs and RVs is shown in Figures 4 (TTVs) and 5 (RVs).

<sup>14</sup> <https://github.com/California-Planet-Search/radvel>

<sup>15</sup> The TTVs constrain  $M_k/M_\star$ , whereas the RVs constrain  $M_k/M_\star^{2/3}$ .

Incorporating the priors in Table 1, we used **emcee** to explore the posteriors and covariances of the dynamical parameters. We ran 100 walkers 10,000 steps each, throwing away the first 4000 steps as burn-in, and found that our chains had converged based on the PSRF statistic. (The inclusion of RV data helped the chains converge faster.) The result of our **emcee** analysis is shown in Figure 6. Our results are summarized in Table 3.

#### 5. INDEPENDENT MULTIPLIED POSTERIORs (IMPS): A QUICK AND DARING WAY TO COMBINE DATASETS

In this section we offer a sanity check of our combined RV+TTV dynamical solution. Since the RVs and TTVs are independent observations, the marginalized posteriors from their separate analyses can be multiplied together to estimate the joint probability distribution of a parameter of interest. This is codified in probability theory as

$$P(A \cap B) = P(A) \times P(B) \quad (4)$$

if A and B are independent events. Assuming that the RV time series is independent of the TTV times series<sup>16</sup>, the posteriors of the RV-only analysis and the TTV-only analysis can be multiplied together to estimate their joint posterior. We call the product of multiplying the posteriors from independent data sets an Independent, Multiplied Posterior (IMP). The IMP loses some of the information of a simultaneous TTV+RV analysis because the RVs and TTVs are interleaved in time, and because any subtle, slight covariances in the posteriors are not captured in the IMP.

In Figure 7, we show the posteriors of the planet masses from the RV-only (S16) and TTV-only (using the N-body integrator) analyses, and the result of multiplying these posteriors together. For planets e and b, the TTVs provide no new information, and so the IMPs reflect the mass posteriors from the RV-only analysis. However, the TTVs alone do measure the mass of planet d. For planet d, the IMP performs as we would expect: it peaks at a value between the RV-only and TTV-only analyses, and its width is narrower than either analysis is alone. The IMP for the mass of planet d gives  $M_d = 13.8 \pm 2.2 M_\oplus$ . This is in good agreement with what we determined in the simultaneous modeling of the RVs+TTVs ( $M_d = 13.6 \pm 2.0 M_\oplus$ ). As expected, the constraint we get from the simultaneous modeling of the RVs+TTVs is slightly tighter than the constraint from the IMP. Also, the result of simultaneous modeling is slightly closer to the RVs-only solution ( $M_d = 12.75 \pm 2.70 M_\oplus$ ) than the TTVs-only solution ( $M_d = 16.1 \pm 3.8 M_\oplus$ ).

In cases where one is computation-limited or short on time, the IMP provides an approximate answer. However, if the posteriors are highly covariant in both data sets, the IMP might grossly overestimate the uncertainties and might also lose accuracy. This method for combining data sets is convenient and potentially useful for combining TTV and/or RV data sets with data from GAIA or WFIRST in the future, but should be used with great caution.

#### 6. DISCUSSION

<sup>16</sup> This is easier to satisfy than the claim that each RV and each TTV is an independent measurement

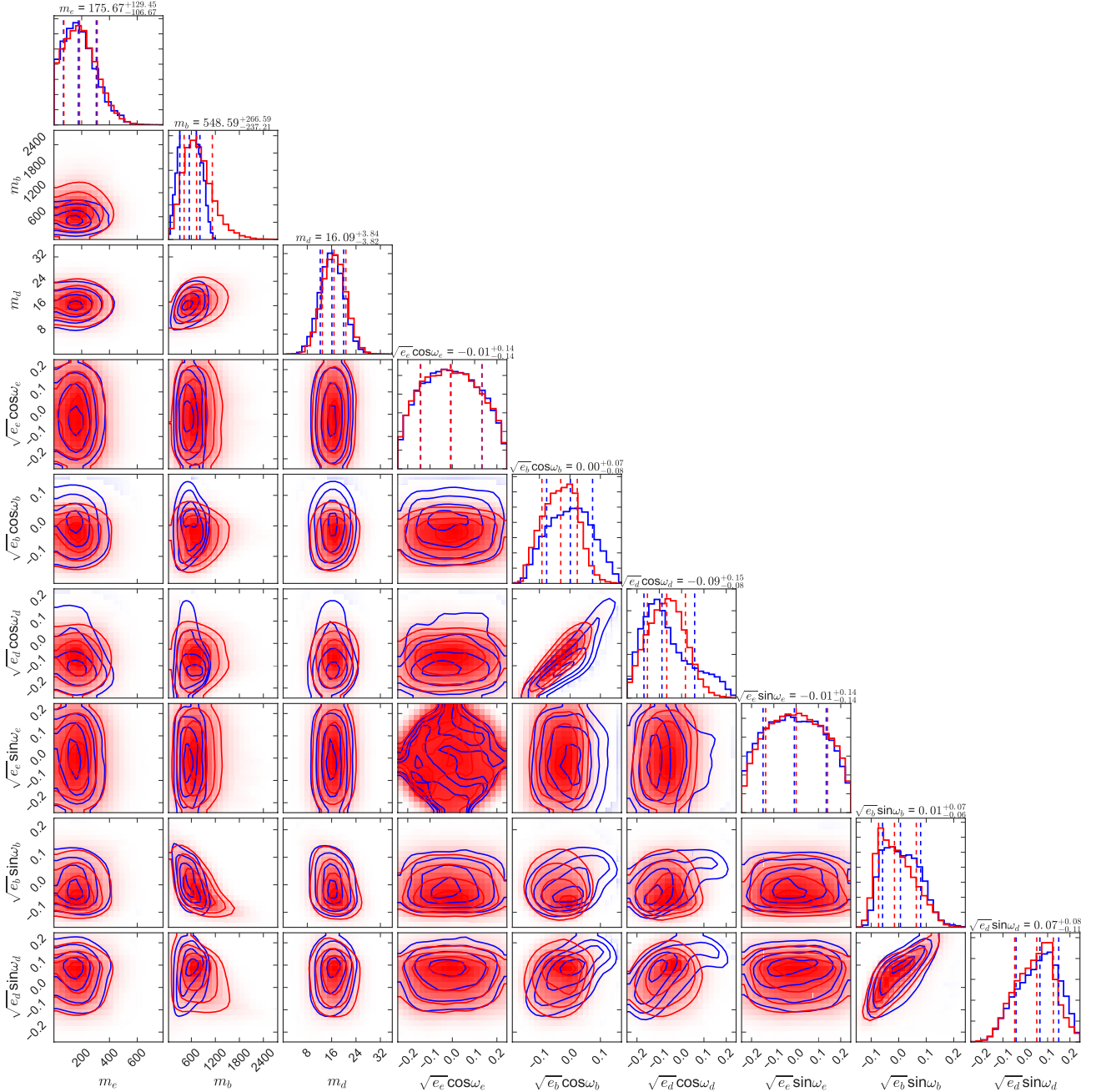


FIG. 3.— The posteriors of the analyses of the TTVs alone. Blue: from the TTVFast N-body integrator MCMC; red: from the analytic TTV modeler TTVFaster MCMC. In both analyses, we limited  $e < 0.06$  for the three inner planets, in accordance with the stability analysis from B15. We also required Hill stability. The mass and eccentricity posteriors obtained from the analytic TTV analysis are in good agreement with those obtained with N-body modeling. The values above the histograms correspond to the N-body posterior median and  $1\sigma$  bounds.

Here we examine how our joint analysis of the WASP-47 TTVs and RVs provides information about the compositions, orbital dynamics, and formation history of the WASP-47 planets.

### 6.1. Relative Information in Dynamical Analyses

Table 4 summarizes the relative information in various dynamical analyses of the planet masses and eccentricities. B15 modeled the K2 TTVs in a 3-planet N-body analysis in which the orbital periods and initial times of transit were fixed, resulting in narrow posteriors for the mass of planet b. The mass constraint for planet e comes

from the choice of prior, rather than the TTVs. B15 also forward-modeled the system for 10 Myr using Mercury (Chambers 1999) to ensure stability, which resulted in the tight eccentricity constraints for the inner planets:  $e_k < 0.06$ .

Almenara et al. (2016, A16 hereafter) did a photodynamical analysis of the K2 TTVs and 71 literature RVs from the PFS and CORALIE spectrographs. The high signal-to-noise of the transits of planet b allowed them to determine stellar limb-darkening parameters and the planet impact parameter very precisely which, in combination with the small eccentricity of planet b, led

TABLE 3  
DYNAMICAL PARAMETERS FROM SIMULTANEOUS FIT TO TTVs  
(TTVFASTER) + RVs (KEPLERIAN)

Parameter	Median $\pm$ Std. Dev.	95% U.L.	Units	Ref.
$M_e$	$9.1 \pm 1.0$		$M_\oplus$	A
$M_b$	$358 \pm 12$		$M_\oplus$	A
$M_d$	$13.6 \pm 2.0$		$M_\oplus$	A
$M_c \sin i_c$	$416 \pm 16$		$M_\oplus$	A
$P_e$	$0.78961 \pm 0.00001$		days	A
$P_b$	$4.15912 \pm 0.00001$		days	A
$P_d$	$9.0304 \pm 0.0003$		days	A
$P_c$	$596 \pm 2$		days	A
$TT_e$	$2146.7641 \pm 0.0007$		BJD - 2454833	A
$TT_b$	$2149.9785 \pm 0.0001$		BJD - 2454833	A
$TT_d$	$2155.308 \pm 0.001$		BJD - 2454833	A
$TT_c$	$1162 \pm 5$		BJD - 2454833	A
$\sqrt{e_e} \cos \omega_e$	$0.01 \pm 0.13$			A
$\sqrt{e_b} \cos \omega_b$	$0.009 \pm 0.03$			A
$\sqrt{e_d} \cos \omega_d$	$-0.01 \pm 0.06$			A
$\sqrt{e_c} \cos \omega_c$	$-0.40 \pm 0.04$			A
$\sqrt{e_e} \sin \omega_e$	$0.07 \pm 0.13$			A
$\sqrt{e_b} \sin \omega_b$	$0.04 \pm 0.04$			A
$\sqrt{e_d} \sin \omega_d$	$0.03 \pm 0.08$			A
$\sqrt{e_c} \sin \omega_c$	$-0.35 \pm 0.06$			A
$M_\star$	$1.00 \pm 0.05$		$M_\odot$	B
$e_e$	$0.03 \pm 0.02$	$0.06^1$		A
$e_b$	$0.0028 \pm 0.0028$	$0.011$		A
$e_d$	$0.007 \pm 0.007$	$0.025$		A
$e_c$	$0.28 \pm 0.02$			A
$e_d \cos \omega_d - e_b \cos \omega_b$	$-0.001 \pm 0.005$			A
$e_d \sin \omega_d - e_b \sin \omega_b$	$0.0 \pm 0.007$			A
$\omega_e$	$81.0 \pm 146.0$		deg.	A
$\omega_b$	$51.0 \pm 82.0$		deg.	A
$\omega_d$	$76.0 \pm 106.0$		deg.	A
$\omega_c$	$138.0 \pm 8.0$		deg.	A
$R_e$	$1.87 \pm 0.13$		$R_\oplus$	B
$R_b$	$13.11 \pm 0.89$		$R_\oplus$	B
$R_d$	$3.71 \pm 0.26$		$R_\oplus$	B
$\rho_e$	$7.7 \pm 1.3$		$\text{g cm}^{-3}$	A
$\rho_b$	$0.88 \pm 0.11$		$\text{g cm}^{-3}$	A
$\rho_d$	$1.5 \pm 0.3$		$\text{g cm}^{-3}$	A

NOTE. — Results from the MCMC analysis of the TTVs + RVs. The columns are: parameter, median value plus-or-minus standard deviation, 95% upper limit (if interesting), and units. The rows above the line are the parameters directly modeled in the MCMC; the rows below the line are derived orbital parameters. A—Derived in this analysis. B—from S16. 1—Note that the upper limit on the eccentricity of planet e is determined from orbital stability requirements, not the measurements.

TABLE 4  
RELATIVE INFORMATION IN LITERATURE DYNAMICAL ANALYSES

Parameter	B15	A16.1	A16.2	S16	TTVs-Nbody	RVs+TTVs
$M_\star [M_\odot]$	$1.04 \pm 0.08$	$1.11^{+0.89}_{-0.49}$	$1.029 \pm 0.031$	$0.99 \pm 0.05$	$0.99 \pm 0.05$	$1.00 \pm 0.05$
$M_e [M_\oplus]$	$< 22^P$	$9.1^{+5.5}_{-2.9}$	$9.1^{+1.8}_{-2.9}$	$9.11 \pm 1.17$	$176 \pm 118$	$9.1 \pm 1.0$
$M_b [M_\oplus]$	$341^{+73}_{-55}$	$383^{+190}_{-120}$	$363.8 \pm 8.6$	$356 \pm 12$	$549 \pm 252$	$358 \pm 12$
$M_d [M_\oplus]$	$15.2 \pm 7$	$16.8^{+12}_{-7}$	$15.7 \pm 1.1$	$12.75 \pm 2.70$	$16.1 \pm 3.8$	$13.6 \pm 2.0$
$M_c [M_\oplus]$	—	$500^{+320}_{-190}$	$470^{+200}_{-100}$	$411 \pm 18$	—	$416 \pm 16$
$e_e$	$< 0.06$	$< 0.11$	—	$= 0^P$	$< 0.06^P$	$< 0.06^P$
$e_b$	$< 0.06$	$< 0.01$	—	$< 0.013$	$< 0.05$	$< 0.01$
$e_d$	$< 0.06$	$< 0.024$	—	$= 0^P$	$< 0.044$	$< 0.025$
$e_c$	—	$0.36 \pm 0.12$	—	$0.27 \pm 0.04$	—	$0.28 \pm 0.02$

NOTE. — B15 - Becker et al. (2015), K2 TTVs, fixed  $P$ ,  $TT$  for each planet, 10 Myr stability enforced. A16.1 - Almenara et al. (2016), photodynamical analysis of K2 TTVs and 71 RVs, A16.2 - including stellar models. S16 - Sinukoff et al. 2016, 118 RVs. TTVs-Nbody - TTVFast N-body analysis (presented herein), K2 TTVs. RVs+TTVs - simultaneous analysis of K2 TTVs and 118 RVs. All upper limits are 95% confidence.  $P$  - results come from a prior.



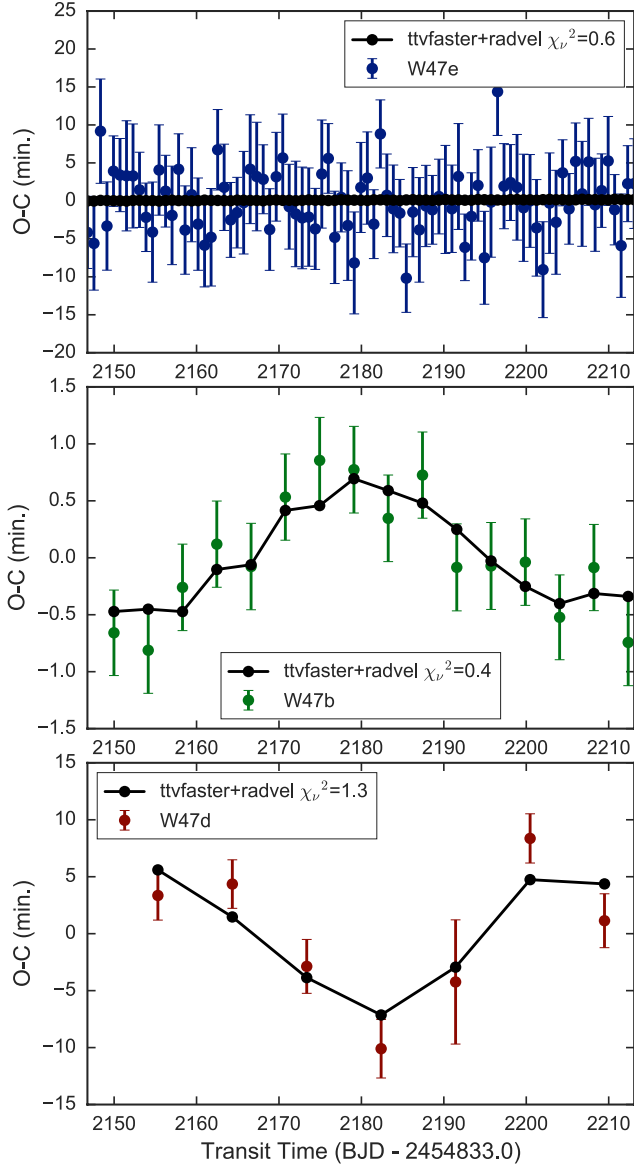


FIG. 4.— The best simultaneous fit to the TTVs and RVs of the WASP-47 system, and residuals. From top to bottom, the panels show the TTVs of the transiting planets e ( $P = 0.79$  days, blue), b ( $P = 4.16$  days, green), and d ( $P = 9.0$  days, brown). The best simultaneous fit to the TTVs + RVs of all four planets is shown as black connected points.

to a very precise determination of the stellar density through asterodensity profiling (Kipping 2014). This led to a model-independent estimate of the planetary masses, presented in column A16.1 of Table 4. By including constraints from the Dartmouth stellar isochrone models (Dotter et al. 2008), the authors were able to constrain the star and planet masses more precisely, but at the expense of accuracy. The model-dependent star and planet masses are shown in column A16.2.

S16 combined 47 new HIRES RVs with the 71 literature RVs. While the CORALIE RVs had provided a long baseline enough baseline to detect non-transiting planet c (Neveu-VanMalle et al. 2016) and the PFS RVs had provided sufficiently high precision to detect a marginal RV signal from planet e (Dai et al. 2015), the HIRES RVs provided both a long baseline and high precision in a sin-

gle dataset. The HIRES data combined with the other RV datasets resulted in smaller uncertainties for all the planet masses than what had been reported in previous RV studies.

Our TTV-only N-body analysis (TTVs-Nbody) and simultaneous RV and TTV analysis (RVs+TTVs) are shown in Table 4. The TTVs-Nbody column illustrates how much information is contained in the TTVs. The RVs+TTVs column illustrates how much information is gained by a joint analysis of the TTVs and RVs. Our RVs+TTVs analysis confirms the precise values obtained by A16 when they include constraints from stellar models (A16.2).

How much information about planet masses comes from the TTVs? As discussed in the TTV-only analysis (see Section 3), the TTVs do not provide much information about the transiting planet masses, with the exception of the mass of planet d, which is constrained through the TTVs of planet b.

Simultaneously modeling the TTVs and RVs of planet d yields a more precise determination of the mass of planet d than can be obtained from either analysis alone: the uncertainties shrink from  $3.8 M_{\oplus}$  (TTVs) and  $2.7 M_{\oplus}$  (RVs) to  $2.0 M_{\oplus}$  (TTVs + RVs). The TTVs provide no information about the mass of planet c, which has a very long period compared to the inner planetary system and thus has no effect on the TTVs. Thus, the RVs provide the majority of the information about planet masses, although the TTVs contribute substantially to the mass measurement of planet d.

The information about planet eccentricities comes from stability constraints, the TTVs, and the RVs. The eccentricity of planet e is not constrained by either the TTVs or the RVs, and so its eccentricity varies from 0 to 0.06 (the upper limit from stability requirements). The RVs constrain  $e_b < 0.013$  (95% confidence, S16). The TTVs constrain  $e_b < 0.02$  (95% confidence), and the combined RVs+TTVs further constrain  $e_b < 0.011$  (95% confidence). The RVs alone do not provide a strong constraint for the eccentricity of planet d (S16 fixed  $e_d = 0$ ). The TTVs alone constrain  $e_d < 0.05$  (95% confidence), and the combined TTVs+RVs constrain  $e_d < 0.025$  (95% confidence). Thus, the TTVs provide additional information about the small eccentricities of planets b and d. The eccentricity of planet c is determined entirely from RVs because the planet is dynamically decoupled from the inner planetary system.

Thus, combining the TTVs and RVs provides more information about masses and eccentricities than either dataset does alone. We discuss the physical importance of the precise measurements of the masses and eccentricities below.

## 6.2. Masses and densities of the planets

WASP-47 is unusual in that the masses of its planets span almost two orders of magnitude. The low-mass planets e and d are shown in a density-radius and mass-radius diptych for small planets (see Figure 8). The lowest-mass planet, WASP-47 e, is  $9.1 \pm 1.0 M_{\oplus}$ . At  $1.9 R_{\oplus}$ , this planet has a density of  $7.7 \pm 1.3 \text{ g cm}^{-3}$ . Planets larger than approximately  $1.5 R_{\oplus}$  are unlikely to be rocky (Weiss & Marcy 2014; Rogers 2015). Yet, planet e is small and dense enough that a rocky composition is possible based on an extrapolation of the empir-



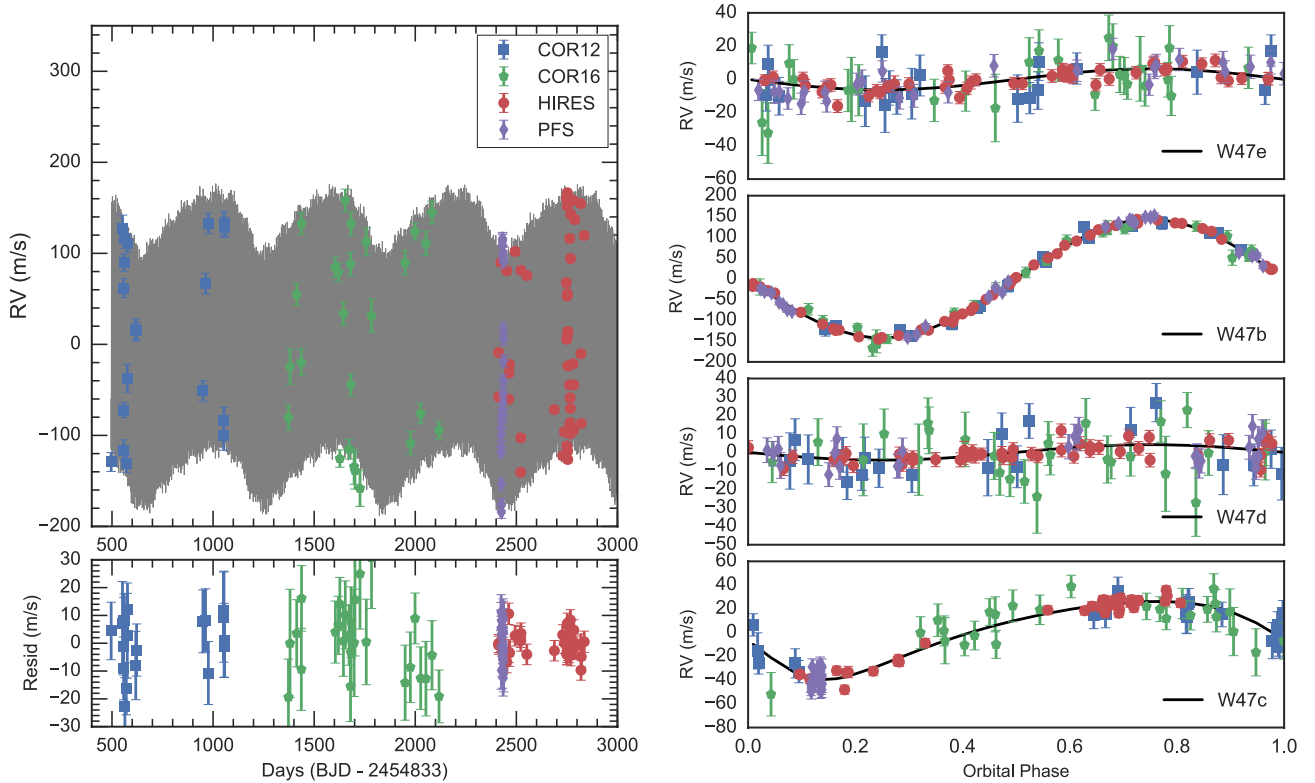


FIG. 5.— Left, top: Radial velocities of WASP-47 from four observational campaigns: CORALIE before 2012 (blue squares), CORALIE before 2016 (green pentagons), PSF (purple diamonds), and HIRES (red circles). The best-fit model to the TTVs and RVs (fine gray line) is shown. Left, bottom: RV residuals (observations minus the *TTVfaster+radvel* model values). The RMS of the residuals is  $8.5 \text{ m s}^{-1}$ , which is comparable to the mean jitter-enhanced RV uncertainty over all the telescopes ( $7.7 \text{ m s}^{-1}$ ). Right: the RVs phase-folded to the orbital periods of planet e (top), b (second from top), d (second from bottom), and c (bottom). The HIRES RVs are the only single dataset that constrain the semi-amplitudes of all the planets, because they have the precision ( $3 \text{ m s}^{-1}$ ) to capture the small amplitudes of planets e and d, and also the baseline to capture the amplitude of the long-period planet c.

ical relationship for rocky planets smaller than  $1.5 R_{\oplus}$  (Weiss & Marcy 2014) and theoretical predictions of planet mass and radius for an Earth-like composition (Seager et al. 2007). However, the density of planet e is also consistent with slightly lower densities that might correspond to a rocky interior overlaid with a thin, low-mass envelope of high mean molecular weight materials. Such a composition has also been hypothesized for 55 Cancri e, which has a very similar mass, radius, and bulk density to WASP-47 e (Lopez 2016, S16).

By contrast, WASP-47 d, which is  $3.7 R_{\oplus}$ , has a mass of  $13.6 \pm 2.0 M_{\oplus}$ . This is a slightly higher mass than was reported in S16 because the TTVs add mass information. The additional information from the TTVs also narrows the mass posterior, shrinking the uncertainty from 2.7 to  $2.0 M_{\oplus}$ . The density of WASP-47 d is  $1.5 \pm 0.3 \text{ g cm}^{-3}$ , making it a high-density member of the population of sub-Neptune sized planets with volatile envelopes. The mass-radius diagram in Figure 8 shows that the mass, radius, and density of WASP-47 d make it one of the most Neptune-like planets discovered to date. While its composition could be explained by a two-layer model of a H/He envelope atop a silicate-iron core, a Neptune-like composition that includes a thick layer of super-ionic water might also explain the bulk properties of WASP-47 d.

WASP-47 b is a Jupiter-mass planet ( $358 \pm 12 M_{\oplus}$ ) that receives  $440 \pm 70$  times as much incident stellar ir-

radiation as the Earth does. At  $13.11 \pm 0.89 R_{\oplus}$ , the planet has a typical density ( $0.88 \pm 0.11 \text{ g cm}^{-3}$ ) for its mass and incident stellar flux (see Figure 9), consistent with various theories (Batygin et al. 2011; Fortney & Nettelmann 2010, and references therein) that stellar irradiation inflates the planet and/or prevents the planet from cooling.

### 6.3. Eccentricities of the planets

The orbits of the three inner planets are profoundly circular. B15 found that eccentricities of  $< 0.06$  were required for stability. Here, we tighten the eccentricities to  $e_b < 0.011$  and  $e_d < 0.025$  (95% confidence). In the highest-eccentricity cases for planets b and d, they tend to be apsidally aligned. We compute  $e_d \cos \omega_d - e_b \cos \omega_b = -0.001 \pm 0.005$  and  $e_d \sin \omega_d - e_b \sin \omega_b = 0.0 \pm 0.007$ .

Although the tidal circularization timescale for planet e is only  $\sim 10^4 - 10^5$  years, depending on the tidal Q value for the planet, our N-body analysis revealed that the neighboring giant planet (b) perturbs the eccentricity of planet e on a timescale 1.26 days. This timescale happens to be related to the orbital periods of both e and b by  $1/P_{\text{kick}} = (1/P_e + 2/P_b)^{-1}$ .

The very low eccentricities of the WASP-47 planets are remarkably like those of the solar system planets (see Figure 10). The average eccentricity of the detected planets in WASP-47 is  $< 0.09$ ; in the solar system, the average eccentricity of the planets and Pluto is 0.08.

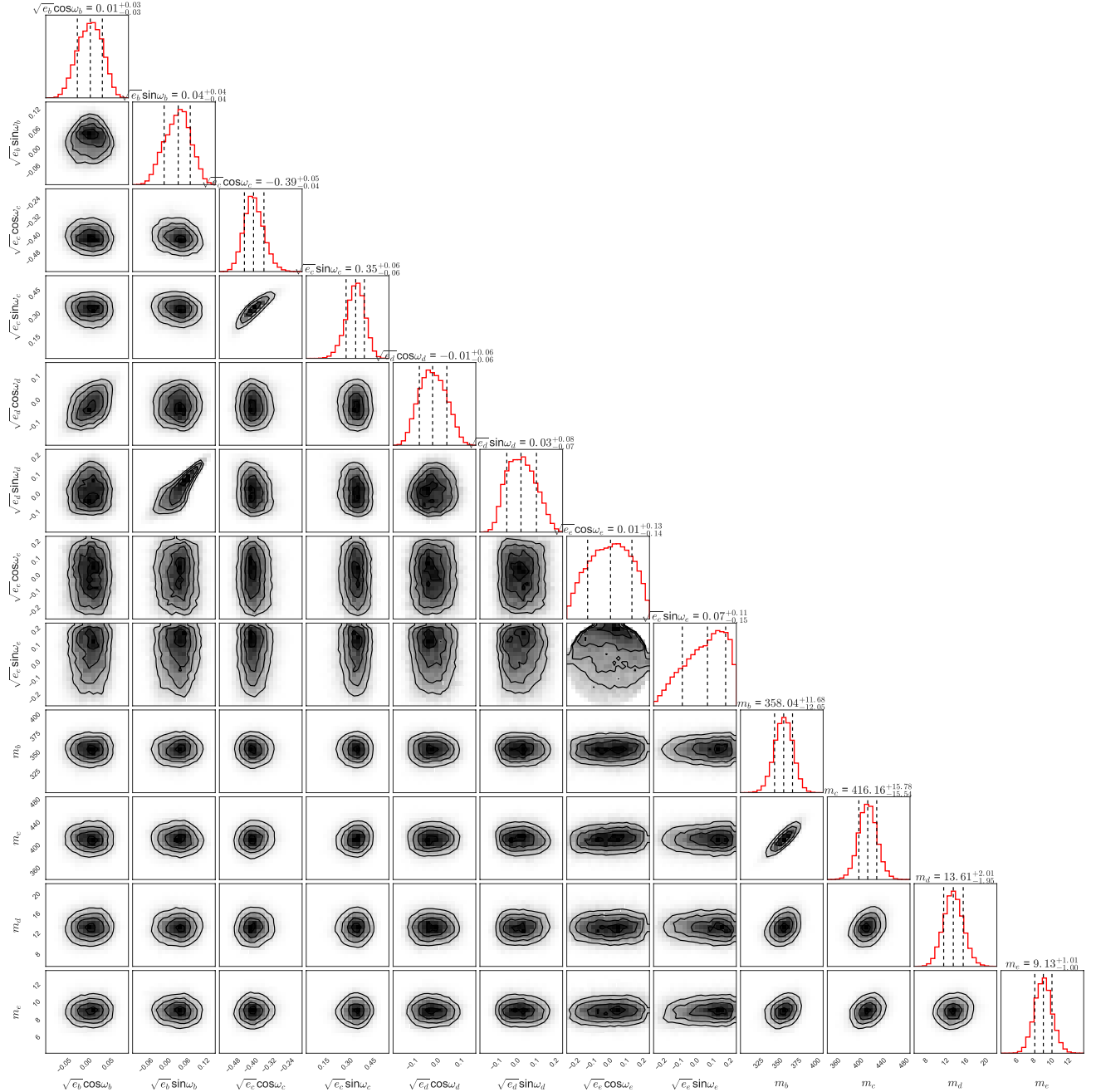


FIG. 6.— The mass and eccentricity posteriors of the WASP-47 planets based on a simultaneous fit to the TTVs and RVs (see Equation 3) using the analytic TTV package **TTVFaster** and the Keplerian RV package **radvel**. The masses, orbital periods, times of transit, eccentricities, and stellar mass were allowed to vary.

#### 6.4. Observational Constraints on Formation Theories

Compact systems like the WASP-47 inner planets might form *in situ* from protoplanetary disks that are more massive than the minimum mass solar nebula (Chiang & Laughlin 2013). Scenarios in which either gas-poor sub-Neptunes or gas-rich Jupiters form *in situ* have been proposed (Lee et al. 2014; Lee & Chiang 2015; Lee & Chiang 2016; Batygin et al. 2016). If all the WASP-47 planets formed *in situ* from the same nebular material, the challenge is to explain how WASP-47 b managed to achieve runaway growth, whereas its immediate neighbors remained gas-poor. Whether a Jupiter-mass or sub-Saturn mass planet forms depends on the core

mass, atmospheric opacity and metallicity, and the disk lifetime (Hori & Ikoma 2011; Venturini et al. 2015). In a gas-rich disk, the atmospheric opacities and metallicities must be finely tuned to prevent cores from accreting more than  $\sim 0.1 M_{\oplus}$  of gas (Lee & Chiang 2016), but such tuning might also prevent the growth of WASP-47 b. However, gas-poor sub-Neptunes are readily formed if the cores form and accrete their envelopes in a gas-poor (transitional) disk. The formation of sub-Neptune cores by giant impact requires at least four orders of magnitude of gas-depletion with respect to the minimum mass extrasolar nebula (Lee & Chiang 2016), leaving  $\sim 0.3 M_{\oplus}$  of gas in the disk. This gas budget is insufficient to form

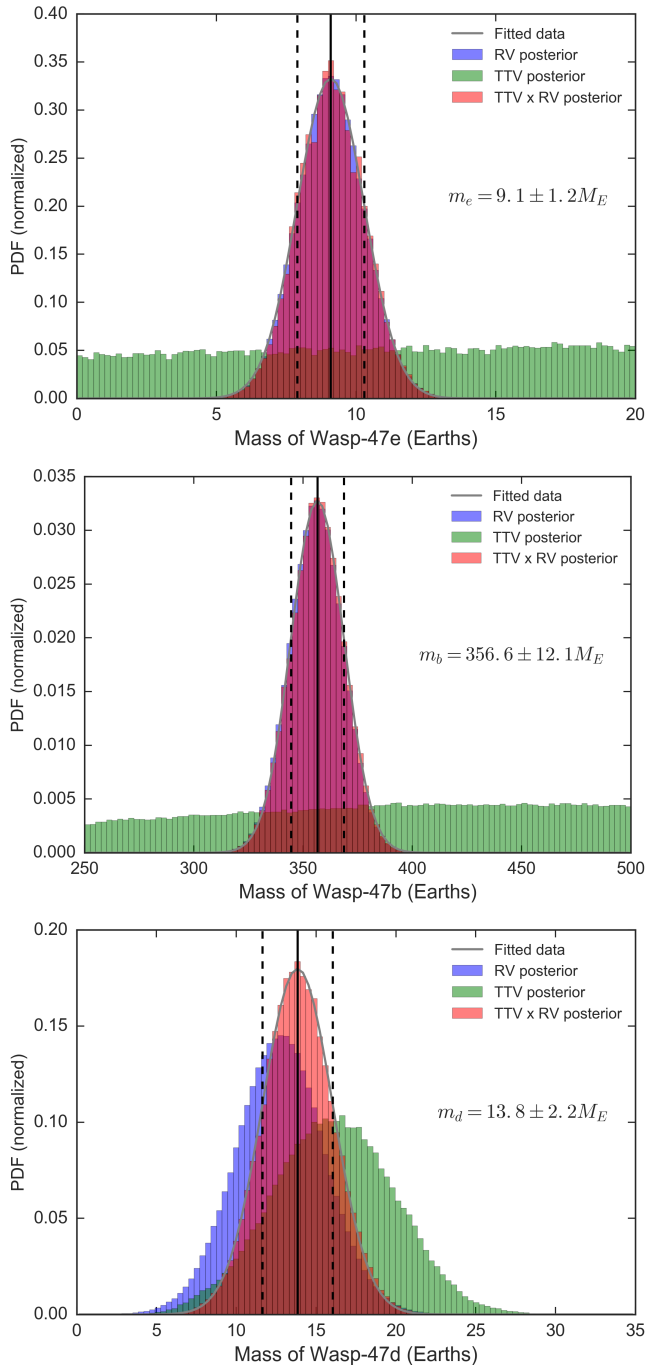


FIG. 7. — Top: posteriors of the mass of WASP-47 e from analyses of the RVs only (blue), the TTVs only (green, using the N-body integrator TTVFast), and their product (i.e. IMP, red). The gray line shows a Gaussian fit to the IMP, with the mean (solid black line) and  $1\sigma$  interval (dashed black lines) shown. Middle: same as the top, but for WASP-47 b. Bottom: same as the top, but for WASP-47 d. Note that the result of computing the IMP for planet d is in good agreement with the simultaneous RV+TTV analysis ( $13.6 \pm 2.0 M_{\oplus}$ ).

the  $\sim 300 M_{\oplus}$  of gas in WASP-47 b.

A modification of in situ formation is inside-out growth via pebble accretion, in which pebbles are transported inward through the disk until they are stopped by a pressure maximum at the boundary between the magnetorotational instability (MRI) zone and the magnetic dead zone (Chatterjee & Tan 2014). At this boundary, the

pebbles may become Toomre unstable or may coalesce via core accretion. As the gas disk clears and the boundary between the MRI and dead zone moves outward, the site of planet formation gradually moves out through the disk. Because the hot Jupiter is situated between two sub-Neptunes, the accretion rate of the disk would likely need to increase by roughly an order of magnitude, and then decrease again, to explain the high mass of the Jupiter compared to its neighbors. Furthermore, the efficacy of forming hot Jupiters via inside-out planet formation has not been well studied.

Alternatively, the planets could have formed elsewhere in the disk and then migrated via interactions with the disk to their present locations. In both Type I and Type II disk migration, the disk damps planet eccentricity, allowing planets to maintain circular orbits in a manner consistent with the nearly circular orbits of the three inner planets. However, slow migration can trap the planets in mean motion resonances. While WASP-47 b and d are near the 2:1 mean motion resonance, they are not trapped. Thus, their migration history must either include a mechanism to prevent planets b and d from entering the 2:1 resonance, or remove them from the resonance (e.g., Adams et al. 2008; Goldreich & Schlichting 2014). In particular, (Deck & Batygin 2015) find that if the inner planet of a pair near a first-order mean motion resonance is the more massive (as is the case for WASP-47 b and d), escape from resonance is unlikely. Furthermore, migration in the disk does not explain the eccentricity of planet c ( $0.28 \pm 0.02$ ). Also, planets e and d would need to migrate through the disk without accreting gas.

Planet-planet scattering and Kozai-Lidov oscillations are big-body (as opposed to gas-and-dust) migration mechanisms that can proceed in the presence or absence of a gas disk. These mechanisms can introduce moderate to high eccentricities in the orbits, potentially accounting for the moderate eccentricity of planet c. Kozai-Lidov oscillations are initiated only when two planets have mutual inclinations of at least  $40^\circ$ . The planets swap angular momentum, causing dramatic variations in the inclinations and eccentricities of the planets over time (Kozai 1962; Lidov 1962). The strongest lines of evidence for past Kozai-Lidov interactions would be (1) an observed large mutual inclination between planet c and the inner solar system, and/or (2) a non-zero obliquity between planet b and the stellar spin axis. Sanchis-Ojeda et al. (2015) ruled out a significant spin-orbit misalignment for planet b, but the degeneracy between stellar  $v \sin i$  and the planet-star obliquity allows moderate misalignments ( $|\lambda| < 48^\circ$  with  $1\sigma$  confidence). If planet c is coplanar and the spin-orbit alignments of the planets are small, a coplanar, high-eccentricity migration scenario such as the one proposed in Petrovich (2015) might best explain the present locations of the planets. However, the current nearly-circular, coplanar orbits of the inner planetary system are not consistent with a past modest eccentricity and/or inclination for planet b. Recall from the stability analysis in B15 that the nearly all of the scenarios in which the eccentricity of planet b exceeds 0.06 become unstable within 10 Myr. Therefore, although high eccentricity migration mechanisms can explain the present positions of planets b and c, such mechanisms would have destroyed the small, close-in planets.

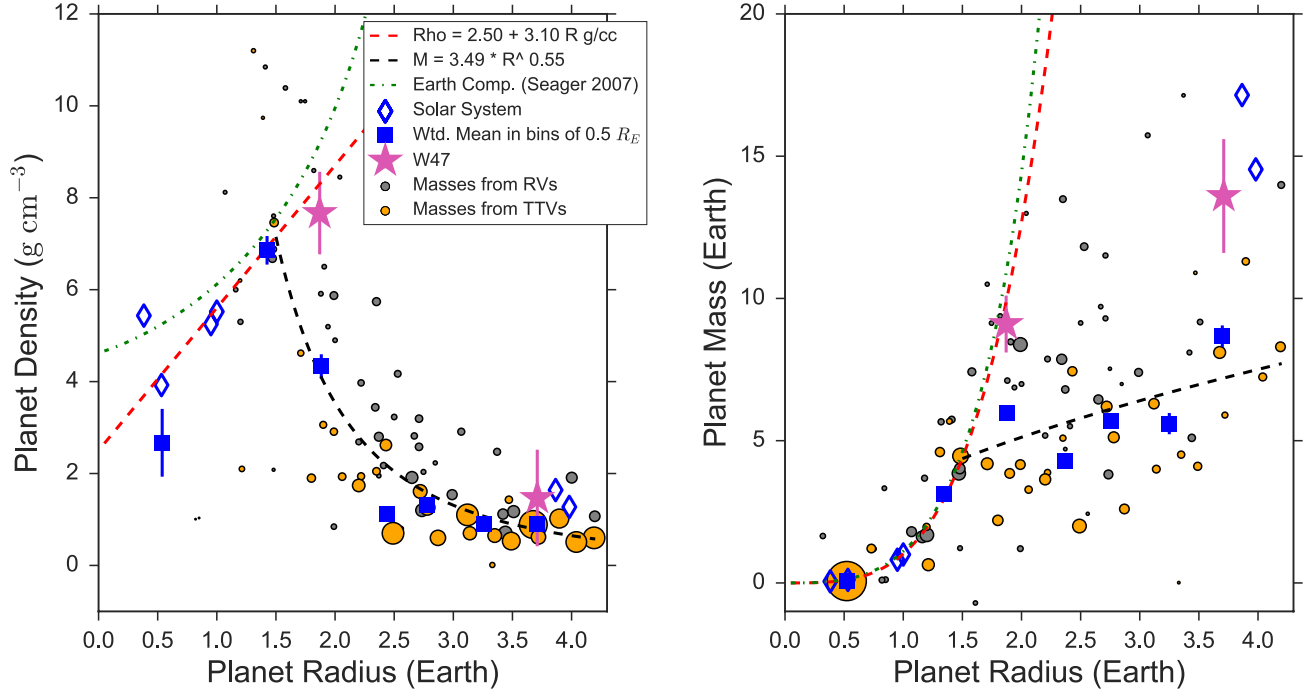


FIG. 8.— Left: planet density versus planet physical radius for 94 transiting planets smaller than  $4.2 R_{\oplus}$ . The gray points have masses determined from RVs; the gold points have masses determined from TTVs. The size of the point corresponds to  $1/\sigma_p^2$ . Blue squares show the weighted mean density in bins of  $0.5 R_{\oplus}$  to guide the eye. The blue diamonds are the solar system planets. The red dashed line is an empirical linear fit to planet density versus radius for the exoplanets and solar system planets smaller than  $1.5 R_{\oplus}$ , extended to predict the densities of potentially rocky planets larger than  $1.5 R_{\oplus}$ . For comparison, we show the predicted density-radius curve for a polytropic equation of state of an Earth-composition planet (Seager et al. 2007, green dotted line). The black line is an empirical power-law fit to planet mass versus radius for planets larger than  $1.5 R_{\oplus}$ . WASP-47 e ( $1.9 R_{\oplus}$ ) sits on the red line and therefore is consistent with a rocky composition, but could also have a thin volatile envelope. WASP-47 d ( $3.7 R_{\oplus}$ ) has a density that requires significant volatiles, including the possibility of high-density volatiles based on the similarity of its bulk properties to Uranus and Neptune. Right: Same as the left panel, but showing planet mass versus radius, and the point sizes correspond to  $1/\sigma_m^2$ .

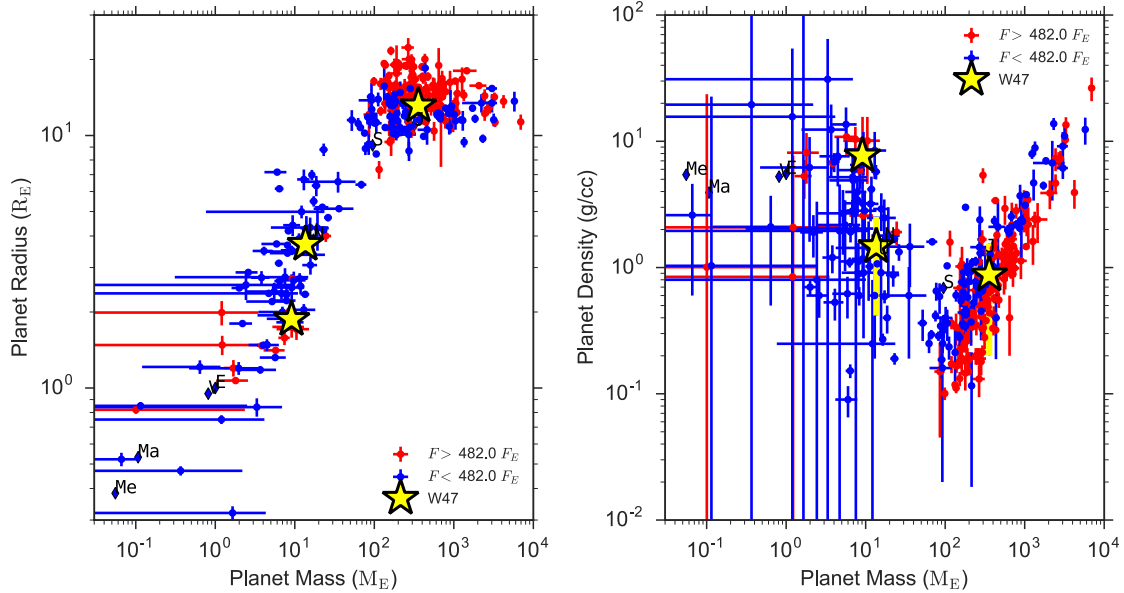


FIG. 9.— Left: planet radius vs. mass for exoplanets with measured masses and radii, as determined by querying exoplanets.org on 2016/05/25. The sample is divided into those that receive more than the median incident flux ( $F > 482 F_{\oplus}$ , red points) and those that receive less than the median incident flux ( $F < 482 F_{\oplus}$ , blue points). The solar system planets are labeled. The WASP-47 planets are shown (yellow stars, the mass and radius error bars are smaller than the symbols). The sub-Neptunes WASP-47 e and d are high-density for their size. WASP-47 b is a typical-sized hot Jupiter for its mass and incident flux.

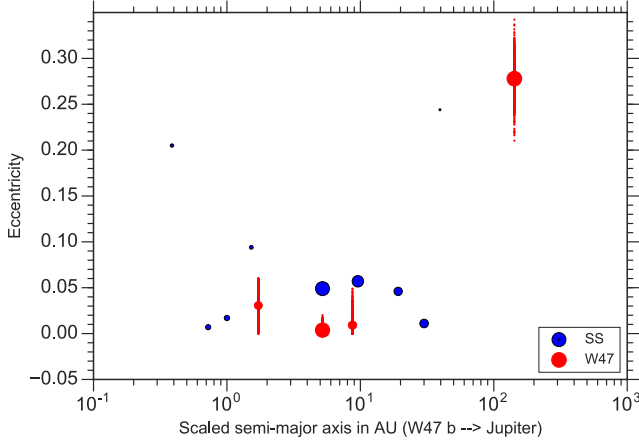


FIG. 10.— The mean eccentricities of the WASP-47 and solar system planets versus the orbital distances, scaled such that  $a_b = a_J$  to facilitate comparison. The point size corresponds to  $M_p^{1/3}$ , to illustrate the mass range while keeping all the planets visible. The spread of each WASP-47 planet eccentricity is illustrated with a cloud of 1000 small red points drawn from the eccentricity posterior. The average eccentricity of the W47 planets is comparable to the average eccentricity of the solar system planets, if we include Pluto.

One way to explain the present orbits and compositions of the WASP-47 planets is that the planets did not all form at the same time. As a point of reference, consider the solar system. In our own solar system, the giant planets must have formed early (within 1 to 10 Myr), when the proto-planetary disk was still gas-rich (de Pater & Lissauer 2001). In contrast, the formation of terrestrial-mass planets by planetesimal accretion can take as long as  $\sim 10^8$  years in N-body simulations and is more efficient in gas-poor disks where the planetesimal eccentricities can grow, leading to more collisions (Lissauer 1987; Pollack et al. 1996; Ida & Lin 2004; Lee & Chiang 2016). Thus, it is possible that the solar system giant planets formed and migrated to their present locations before the terrestrial planets formed. The Nice Model demonstrates that early formation and migration of the Jupiter and Saturn can reproduce the current orbital architectures, compositions, and impact histories of the gas giants, ice giants, terrestrial planets, and Trojan asteroids (Tsiganis et al. 2005; Gomes et al. 2005; Morbidelli et al. 2005). The Grand Tack Model shows that a reversal in the direction of Jupiter’s migration due to Saturn can explain the small size of Mars and detailed compositional features of the asteroids (Walsh et al. 2011; Morbidelli et al. 2012). Both of these models feature two stages of planet formation:

1. Early giant planet growth combined with disk and/or planet-induced migration produces the current compositions of giant planets and sculpts the radial distribution of planetesimals.
2. When or after the gas disk clears, planetesimal accretion proceeds in the sculpted planetesimal disk, resulting in the formation of low-mass, predominantly rocky planets.

Likewise, the formation and evolution of the planets in WASP-47 might be best explained by a two-stage process. The giant planets in the WASP-47 system might

have formed early in the gas-rich disk and exchanged energy with each other and/or additional bodies and/or the disk to migrate to their present locations. Since planet c has modest eccentricity ( $0.28 \pm 0.02$ ), it almost certainly had some sort of planet-planet interaction in the past, either with planet b or with a still undetected planet. Although it is possible for instabilities in the gas disk to excite giant planet eccentricities, the threshold where this effect operates is  $e < 0.01$  and therefore cannot explain the eccentricity of planet c. It is worth noting that planet b (which has  $e_b < 0.011$ ) could have formed *in situ* in the gas-rich disk, and this scenario requires another massive body to exchange momentum with planet c. On the other hand, if planet b was involved in high-eccentricity migration, drag from the gas disk and/or tidal circularization would have quickly circularized its orbit. The timescale for eccentricity damping due to tides (Murray & Dermott 2000, Equation 4.198) is:

$$\tau_e = -\frac{e}{\dot{e}} = \frac{4}{63} \frac{M_\star}{M_p} \left(\frac{a}{C_s}\right)^5 \frac{\mu_s Q_s}{n}. \quad (5)$$

where  $e$  is the eccentricity,  $M_p$  is the planet mass,  $a$  is the semi-major axis,  $C_s$  is the satellite radius,  $\mu_s$  is the ratio of the elastic to gravitational forces  $\approx (10^4 \text{ km}/C_s)^2$ , and  $Q_s$  is the tidal dissipation factor. For  $a = 0.05 \text{ AU}$  and  $Q_s = 10^{6.5}$  (typical for hot Jupiters, Jackson et al. 2008), the circularization time is  $\tau_e \approx 10^8 \text{ yr}$ . If the gas disk cleared while WASP-47 b and c were finishing their migration, the final years of the giant planets’ migration could have influenced the solid material in the disk, exciting protoplanetary solids to higher eccentricities and inducing a second stage of core accretion. Such an epoch could have formed WASP-47 e and d, and perhaps additional yet-undetected low-mass planets dominated by rocky interiors.

A two-stage formation mechanism might also best explain the current architectures of other multi-planet systems with diverse planet compositions, such as 55 Cancri and Kepler-89 (KOI-94). An improved census of giant planets accompanying the low-mass planetetary systems discovered by *Kepler* will enable studies of the occurrence of planetary systems with diverse compositions like our solar system, illuminating the dominant physical processes in their formation.

Possible evidence of two-stage planet formation in WASP-47 could include:

1. a large mutual inclination between WASP-47 b and c, indicating past Kozai-Lidov interactions,
2. a moderate misalignment between the orbital plane of WASP-47 b and the stellar spin axis, indicating past Kozai-Lidov interactions,
3. a water-rich atmosphere for WASP-47 b, indicating formation beyond the snow line<sup>17</sup>,
4. a water-poor atmosphere for WASP-47 e and d, indicating formation inside the snow line.

Continued observations of this system and other systems with diverse planet compositions from the James

<sup>17</sup> Other low-temperature condensate molecules like carbon monoxide and carbon dioxide could be present instead of water.



Webb Space Telescope, the WFIRST mission, and other facilities will provide evidence for or against a two-stage planet formation scenario.

## 7. CONCLUSION

We combine 118 RVs and 108 K2 TTVs to present some of the most precise masses, densities, and orbital dynamics of the WASP-47 planetary system to date. For the transiting inner planetary system, we obtain  $M_e = 9.1 \pm 1.0 M_\oplus$  ( $\rho_e = 7.7 \pm 1.3 \text{ g cm}^{-3}$ ),  $M_b = 358 \pm 12 M_\oplus$  ( $\rho_b = 0.88 \pm 0.11 \text{ g cm}^{-3}$ ), and  $M_d = 13.6 \pm 2.0 M_\oplus$  ( $\rho_d = 1.5 \pm 0.3 \text{ g cm}^{-3}$ ).

We place tight upper limits on the eccentricities of the three inner planets:  $e_e < 0.06$ ,  $e_b < 0.011$ , and  $e_d < 0.025$  (95% confidence). The mean eccentricity of the WASP-47 planets (0.09) is very similar to the mean eccentricity of the solar system planets plus Pluto (0.08).

Of the four planets, only WASP-47 e has bulk properties consistent with a rocky composition. WASP-47 d is a sub-Neptune sized planet that is just a little smaller than Neptune but has the density of Neptune, meaning that its bulk properties consistent with a Neptune-like composition. However, WASP-47 d could also be a rocky interior overlaid with a hydrogen-rich, water-poor envelope. WASP-47 b is a hot Jupiter with a typical size for its mass and incident stellar flux.

The non-resonant architecture, diverse masses, and profoundly circular orbits in the WASP-47 resemble our own solar system. We briefly review the highlights of *in situ* planet formation, inside-out planet formation, disk migration, and high-eccentricity migration, noting that

none of these mechanisms alone can reproduce all the physical attributes of the WASP-47 system. We propose that WASP-47, like the solar system, formed in two stages. In stage one, the giant planets formed in a gas-rich disk and migrated via disk and/or high-eccentricity migration to their present locations. In stage two, the high-density sub-Neptunes formed *in situ* in a gas-poor environment.

L. M. W. acknowledges the Trottier Family Foundation for their support. K. D. acknowledges the support of the JCPA fellowship at Caltech. E. S. is supported by a post-graduate scholarship from the Natural Sciences and Engineering Research Council of Canada. E. A. acknowledges support from NASA grants NNX13AF20G, NNX13AF62G, and NASA Astrobiology Institutes Virtual Planetary Laboratory, supported by NASA under cooperative agreement NNH05ZDA001C. A. W. H. acknowledges support from a NASA Astrophysics Data Analysis Program grant, support from the K2 Guest Observer Program, and a NASA Key Strategic Mission Support Project. The authors thank Geoff Marcy, Eva Culakova, Daniel Fabrycky, Jack Lissauer, Jason Rowe, the Kepler-TTV working group, and the KITP Planet Formation and Dynamics workshop for useful discussions. We thank NASA and the Kepler team for the outstanding photometry that contributed to this paper. The authors wish to extend special thanks to those of Hawaiian ancestry on whose sacred mountain of Maunakea we are privileged to be guests. Without their generous hospitality, the Keck observations analyzed herein would not have been possible.

## REFERENCES

- Adams, F. C., Laughlin, G., & Bloch, A. M. 2008, *ApJ*, 683, 1117  
 Agol, E., & Deck, K. 2016a, *ApJ*, 818, 177  
 —. 2016b, TTVFaster: First order eccentricity transit timing variations (TTVs), Astrophysics Source Code Library, ascl:1604.012  
 Almenara, J. M., Díaz, R. F., Bonfils, X., & Udry, S. 2016, *A&A*, 595, L5  
 Batalha, N. M., Rowe, J. F., Bryson, S. T., et al. 2013, *The Astrophysical Journal Supplement Series*, 204, 24  
 Batygin, K., Bodenheimer, P. H., & Laughlin, G. P. 2016, *ApJ*, 829, 114  
 Batygin, K., Stevenson, D. J., & Bodenheimer, P. H. 2011, *ApJ*, 738, 1  
 Becker, J. C., Vanderburg, A., Adams, F. C., Rappaport, S. A., & Schwengeler, H. M. 2015, *ApJ*, 812, L18  
 Borucki, W. J., Koch, D. G., Brown, T. M., et al. 2010, *ApJ*, 713, L126  
 Brooks, S. P., & Gelman, A. 1998, *Journal of computational and graphical statistics*, 7, 434  
 Bryan, M. L., Knutson, H. A., Howard, A. W., et al. 2016, *ApJ*, 821, 89  
 Burke, C. J., Christiansen, J. L., Mullally, F., et al. 2015, *ApJ*, 809, 8  
 Chambers, J. E. 1999, *MNRAS*, 304, 793  
 Chatterjee, S., & Tan, J. C. 2014, *ApJ*, 780, 53  
 Chiang, E., & Laughlin, G. 2013, *Monthly Notices of the Royal Astronomical Society*, 431, 3444  
 Dai, F., Winn, J. N., Arriagada, P., et al. 2015, *ApJ*, 813, L9  
 de Pater, I., & Lissauer, J. J. 2001, *Planetary Sciences*, 544  
 Deck, K. M., Agol, E., Holman, M. J., & Nesvorný, D. 2014, *The Astrophysical Journal*, 787, 132  
 Deck, K. M., & Batygin, K. 2015, *ApJ*, 810, 119  
 Dotter, A., Chaboyer, B., Jevremović, D., et al. 2008, *ApJS*, 178, 89  
 Dressing, C. D., Adams, E. R., Dupree, A. K., Kulesa, C., & McCarthy, D. 2014, *arXiv:arXiv:1407.1848v1*  
 Fabrycky, D. C., Lissauer, J. J., Ragozzine, D., et al. 2014, *ApJ*, 790, 146  
 Fang, J., & Margot, J.-L. 2012, *ApJ*, 761, 92  
 Foreman-Mackey, D., Hogg, D. W., Lang, D., & Goodman, J. 2013, *PASP*, 125, 306  
 Fortney, J. J., & Nettelmann, N. 2010, *Space Sci. Rev.*, 152, 423  
 Fressin, F., Torres, G., Charbonneau, D., et al. 2013, *The Astrophysical Journal*, 766, 81  
 Gelman, A., & Rubin, D. B. 1992, *Statist. Sci.*, 7, 457  
 Gladman, B. 1993, *Icarus*, 106, 247  
 Goldreich, P., & Schlichting, H. E. 2014, *AJ*, 147, 32  
 Gomes, R., Levison, H. F., Tsiganis, K., & Morbidelli, A. 2005, *Nature*, 435, 466  
 Hellier, C., Anderson, D. R., Collier Cameron, A., et al. 2012, *MNRAS*, 426, 739  
 Hori, Y., & Ikoma, M. 2011, *MNRAS*, 416, 1419  
 Howard, A. W., Marcy, G. W., Bryson, S. T., et al. 2012, *ApJS*, 201, 15  
 Ida, S., & Lin, D. N. C. 2004, *ApJ*, 604, 388  
 Jackson, B., Greenberg, R., & Barnes, R. 2008, *ApJ*, 678, 1396  
 Kipping, D. M. 2014, *MNRAS*, 440, 2164  
 Koch, D. G., Borucki, W. J., Rowe, J. F., et al. 2010, *ApJ*, 713, L131  
 Kozai, Y. 1962, *AJ*, 67, 591  
 Lee, E. J., & Chiang, E. 2015, *ApJ*, 811, 41  
 Lee, E. J., & Chiang, E. 2016, *The Astrophysical Journal*, 817, 90  
 Lee, E. J., Chiang, E., & Ormel, C. W. 2014, *ApJ*, 797, 95  
 Lidov, M. L. 1962, *Planet. Space Sci.*, 9, 719  
 Lissauer, J. J. 1987, *Icarus*, 69, 249  
 Lissauer, J. J., Marcy, G. W., Rowe, J. F., et al. 2012, *ApJ*, 750, 112  
 Lissauer, J. J., Marcy, G. W., Bryson, S. T., et al. 2014, *ApJ*, 784, 44  
 Lopez, E. D. 2016, *ArXiv e-prints*, arXiv:1610.01170  
 Morbidelli, A., Levison, H. F., Tsiganis, K., & Gomes, R. 2005, *Nature*, 435, 462

- Morbidelli, A., Lunine, J. I., O'Brien, D. P., Raymond, S. N., & Walsh, K. J. 2012, *Annual Review of Earth and Planetary Sciences*, 40, 251
- Murray, C. D., & Dermott, S. F. 2000, in *Solar System Dynamics* (Cambridge University Press), 321–408, *cambridge Books Online*
- Neveu-VanMalle, M., Queloz, D., Anderson, D. R., et al. 2016, *A&A*, 586, A93
- Newville, M., Stensitzki, T., Allen, D. B., & Ingargiola, A. 2014, *LMFIT: Non-Linear Least-Square Minimization and Curve-Fitting for Python*, doi:10.5281/zenodo.11813
- Petigura, E. A., Howard, A. W., & Marcy, G. W. 2013a, *Proceedings of the National Academy of Sciences*, 110, 19273
- Petigura, E. A., Marcy, G. W., & Howard, A. W. 2013b, *ApJ*, 770, 69
- Petrovich, C. 2015, *ApJ*, 805, 75
- Pollack, J. B., Hubickyj, O., Bodenheimer, P., et al. 1996, *Icarus*, 124, 62
- Rogers, L. a. 2015, *ApJ*, 801, 41
- Rowe, J. F., Bryson, S. T., Marcy, G. W., et al. 2014, *ApJ*, 784, 45
- Sanchis-Ojeda, R., Rappaport, S., Winn, J. N., et al. 2013, *The Astrophysical Journal*, 774, 54
- Sanchis-Ojeda, R., Winn, J. N., Dai, F., et al. 2015, *ApJ*, 812, L11
- Seager, S., Kuchner, M., HierâARajumder, C. a., & Militzer, B. 2007, *The Astrophysical Journal*, 669, 1279
- Steffen, J. H., Ragozzine, D., Fabrycky, D. C., et al. 2012, *Proceedings of the National Academy of Science*, 109, 7982
- Tsiganis, K., Gomes, R., Morbidelli, A., & Levison, H. F. 2005, *Nature*, 435, 459
- Venturini, J., Alibert, Y., Benz, W., & Ikoma, M. 2015, *A&A*, 576, A114
- Walsh, K. J., Morbidelli, A., Raymond, S. N., O'Brien, D. P., & Mandell, A. M. 2011, *Nature*, 475, 206
- Weiss, L. M., & Marcy, G. W. 2014, *ApJ*, 783, L6